CHEMISTRY OF MATERIALS

ARTICLE

pubs.acs.org/cm

Investigation of Microstructural and Electrochemical Properties of Impregnated (La,Sr)(Ti,Mn)$O_{3\pm\delta}$ as a Potential Anode Material in High-Temperature Solid Oxide Fuel Cells

Jung Hyun Kim,[†,‡] David Miller,[‡] Harald Schlegl,[‡] Damien McGrouther,[§] and John T. S. Irvine*[,‡]

[†]Department of Applied Materials Engineering, Hanbat National University, San 16-1, Dukmyung-Dong, Yusung-Gu, Daejeon, 305-719, South Korea

[‡]School of Chemistry, University of St. Andrews, North Haugh, St Andrews, Fife, KY16 9ST, Scotland, United Kingdom

[§]SUPA, School of Physics and Astronomy, University of Glasgow, G12 8QQ, United Kingdom

ABSTRACT: The microstructural and electrochemical properties of $La_{0.4}Sr_{0.6}Ti_{0.8}Mn_{0.2}O_{3\pm\delta}$ (LSTM) fabricated via liquid-phase impregnation have been investigated for solid oxide fuel cell (SOFC) applications. Scanning electron micrography (SEM) showed that LSTM uniformly covers the porous scaffold when heated in an oxidizing atmosphere, which transforms to fine particles when reduced. The electrical conductivity of a 10 wt % CeO_2−50 wt % LSTM−8 mol % yttria-stabilized zirconia (8YSZ) composite anode was higher than that of a 50 wt % LSTM−8YSZ anode and was stable at 700, 800, and 900 °C under reducing conditions. When the 50 wt % LSTM-8YSZ was used as an anode, power densities of the sample were <100 mW cm^{-2} over the entire measured temperature range. The addition of 10 wt % of CeO_2 and 1 wt % of Pd as catalysts increased the power density to 150 and 210 mW cm^{-2} at 800 and 850 °C, respectively.

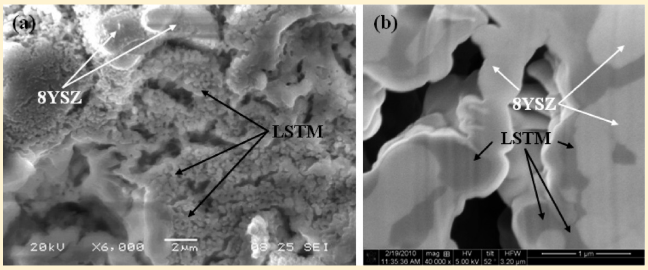

KEYWORDS: solid oxide fuel cell, anode, impregnation, tape cast, dual beam focused ion beam

1. INTRODUCTION

Solid oxide fuel cells (SOFCs) are energy conversion devices that change the chemical energy of hydrogen and oxygen directly into electrical work.[1] Generally, SOFC studies have focused on the development of cathode, anode, and electrolyte materials, because the overpotential from these three elements can be a major source of voltage loss in SOFCs and becomes increasingly important as SOFC operating temperatures decrease.[2−5]

Generally, nickel and yttria-stabilized zirconia (YSZ) have been preferred as anode materials for SOFCs, because the Ni-YSZ cermet anode shows excellent performance while operating using hydrogen as a fuel.[6,7] However, Ni-YSZ anodes are known to undergo degradation due to sulfur poisoning, carbon deposition, and mechanical instability when hydrocarbon-containing fuels have been used.[8−12]

Increasingly, hydrocarbon fuels are being used for SOFC applications, and, although there are several strategies for the prevention and mitigation of degradation in Ni-YSZ anodes,[13−16] new anode materials with good electrochemical properties and resistance to carbon formation are being developed. These materials can be divided into four types of anode for SOFCs, as presented in Table 1.[17−41] One option is to modify the Ni-YSZ cermet by altering the nickel or YSZ, adding oxide material-catalysts, and carrying out surface treatment.[17−35] A second option for alternative anodes is to synthesize new single-phase anode materials, such as perovskite oxides.[25,36−38] The third method is achieved by adding additional catalyst materials. Catalyst-oxide and catalyst-metal-oxide systems have been used to control the carbon formation and enhance the power density.[39,40] Finally, the impregnation of novel alloys or oxides into preformed YSZ substrate skeletons has been shown to allow direct oxidation of the supplied fuel.[41]

A recent study describes the electrochemical properties of $La_{0.75}Sr_{0.25}Cr_{0.5}Mn_{0.5}O_3$ (LSCM) impregnated into a porous YSZ scaffold under humidified H_2 and methane gas, using small amounts of CeO_2 and Pd as catalysts.[42] The changes in structure and conductivity that occur under reducing conditions was investigated.[43] The dense LSCM layer that formed after sintering at 1200 °C under air was observed to change into interconnected nanoparticles covering the YSZ scaffold upon reduction under SOFC anode conditions. Pd and CeO_2 both enhance the electrocatlytic performance for H_2 oxidation, and they, indeed, are known to act in a complementary manner.[44]

In a separate study, the effect of manganese content on the microstructure of the series of potential SOFC anode compounds $La_{0.33}Sr_{0.67}Ti_xMn_{1-x}O_{3\pm\delta}$ ($x = 0.33, 0.5,$ and 0.67) was investigated. The manganese content was found to have a significant effect on the microstructure.[43] As with LSCM, the morphology of these compounds was found to undergo a transformation into nanostructures upon reduction. The

Received: March 13, 2011
Revised: August 2, 2011
Published: August 16, 2011

Table 1. Summary of Alternative Anode Material Strategies for Solid Oxide Fuel Cells (SOFCs)[a]

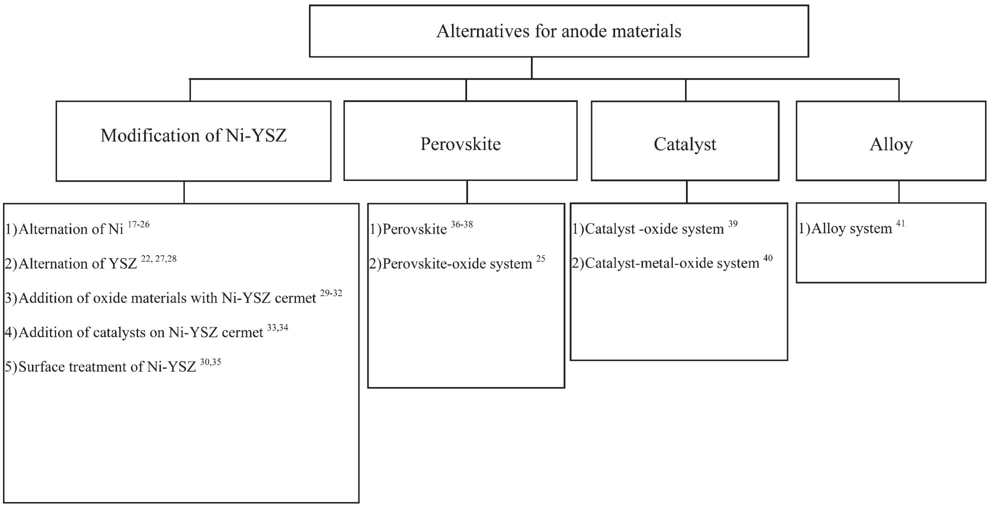

[a] Data taken from refs 17−41.

thermal stability of these structures was observed to improve with decreasing manganese content.

The objective of this work was to further the understanding of lanthanum strontium titanates with low manganese contents by the investigation of the potential SOFC anode material $La_{0.4}Sr_{0.6}Ti_{0.8}Mn_{0.2}O_{3\pm\delta}$ (LSTM). The study focuses on the microstructure and electrochemical properties of an SOFC anode produced by the impregnation of LSTM into YSZ.

2. EXPERIMENTAL SECTION

The SOFCs for this study were produced by tape casting. The SOFCs comprised of two porous layers for anode and cathode skeletons and one dense layer for the 8YSZ electrolyte. For the porous layers, the weight ratio of 8 mol % yttria-stabilized zirconia (8YSZ) and carbon pore former was 1:3 in a methyl ethyl ketone (MEK) and ethanol solution. After preparing the 8YSZ tape with two porous layers using tape casting, these three tapes were cut with a punch and laminated. The green tapes were sintered at 1400 °C for 5 h on an alumina plate with a ramp rate of 1 K min^{-1}. After sintering, the thickness of the dense 8YSZ electrolyte and porous anode layer was ~50 μm, while that of the porous cathode was ~300 μm.

After fabricating SOFC single-cell structures, the nitrate solutions for anode and cathode impregnation were prepared. In this study, $La_{0.4}Sr_{0.6}Ti_{0.8}Mn_{0.2}O_{3\pm\delta}$ (LSTM) was chosen for the anode and $La_{0.8}Sr_{0.2}MnO_3$ (LSM) was chosen for the cathode. The cathode solution for impregnation was prepared from $La(NO_3)_3\cdot6H_2O$ (Alfa Aesar, ACS 99.9%), $Sr(NO_3)_2$ (Alfa Aesar, ACS 99.0%), and $Mn(NO_3)_2\cdot4H_2O$ (Alfa Aesar, ACS 99.98%) dissolved in deionized water with a metal-ion ratio of 0.8:0.2:1.0. The anode solution for LSTM was prepared from $La(NO_3)_3\cdot6H_2O$, $Sr(NO_3)_2$, and $Mn(NO_3)_2\cdot4H_2O$ for La, Sr, and Mn precursors and $(CH_3CH(O^-)CO_2\cdot NH_4)_2{-}Ti(OH)_2$ (dihydroxy-bis-ammonium, lactate, titanium(IV), Alfa Aesar) as the Ti precursor dissolved in deionized water in the appropriate molar ratios to give concentrations of 0.1 g L^{-1}. The precursors were observed to dissolve readily. In the case of the LSTM solution, citric acid was not used, because the Ti precursor acted to stabilize the solution. Separate 0.1 g L^{-1} solutions of $Ce(NO_3)_3\cdot6H_2O$ and $(NH_3)_4Pd(NO_3)_2$ in deionized water were also prepared.

To impregnate the porous anode structure, the LSTM precursor solution was slowly dropped onto the surface of the porous electrode using a syringe. When the structure became saturated with solution, the cell was heated to 500 °C in air to evaporate the solvent. This process was repeated many times until the desired weight of LSTM precursor was reached. The cells were then calcined at 1200 °C for 4 h. This process was then repeated for the LSM cathode. For LSM, the electrode was heated to 400 °C between impregnation steps for drying and was calcined at 1000 °C for 4 h. Additions of CeO_2 and Pd at the anode were impregnated in separate stages. In each case, the drying temperature was 500 °C, and they were not calcined.

The structure and the phase stability of the synthesized LSTM were characterized by powder X-ray diffraction (XRD). The measurements were performed on a Philips Model PW1050 diffractometer operated at 40 kV and 30 mA using Cu Kα radiation. Phases were identified via comparison with previous studies.[43]

The microstructure of the single cells was investigated with a JEOL Model JSM 5600 scanning electron microscopy (SEM) system that was equipped with an Oxford Inca X-ray energy-dispersive spectrometry (EDX) device.

Additional microstructural analysis and preparation of a sample for transmission electron microscopy (TEM) was carried out using a FEI Nova Nanolab 200 Dualbeam FIB/SEM, equipped with a Ga^+ focused-ion-beam (FIB) source operating at 30 keV. As a first step, a protective platinum strap was deposited by FIB-induced deposition from a platinum-containing precursor gas injected by a gas needle near the region of interest. The purpose of this strap was to preserve the top surface and to prevent FIB "curtaining" effects. The FIB was used to mill cross-section trenches at a moderate beam current ($\geq$1 nA), followed by polishing of the trench face at lower currents (< 1 nA). The SEM column, oriented at 52° to the FIB column, was then immediately able to visualize the cross-section face. SEM images were acquired with an electron beam acceleration of 5 keV in secondary-electron collection mode. A TEM sample was prepared via a method similar to that detailed above. In this case, a suitable section of the cell containing both the electrolyte and anode microstructure was identified. Here, two trenches were milled from the material using the ion beam, leaving a thin slice of electron-transparent material. This was then cut from the specimen using the ion beam and attached to a copper grid.

TEM analysis of the FIB-prepared specimen was carried out using a JEOL Model JEM-2011 TEM microscope operating at 200 kV equipped with an Oxford Link Isis X-ray EDX system.

For electrical conductivity measurements, 8YSZ bars were pressed in a rectangular die (4.5 mm × 3 mm × 14.5 mm) and sintered at 1400 °C

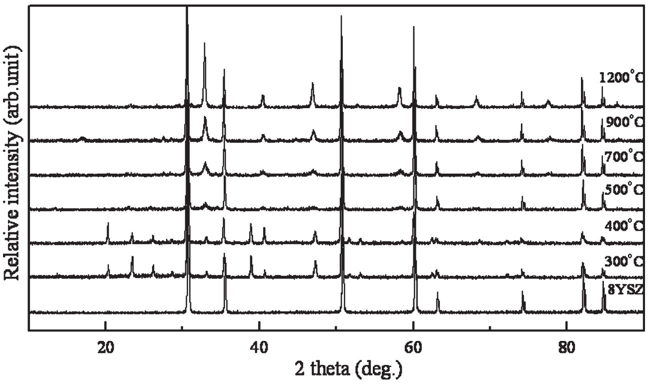

Figure 1. X-ray diffraction (XRD) results of $La_{0.4}Sr_{0.6}Ti_{0.8}Mn_{0.2}O_{3\pm\delta}$ (LSTM) impregnated into a porous 8YSZ scaffold, relative to the calcination temperature.

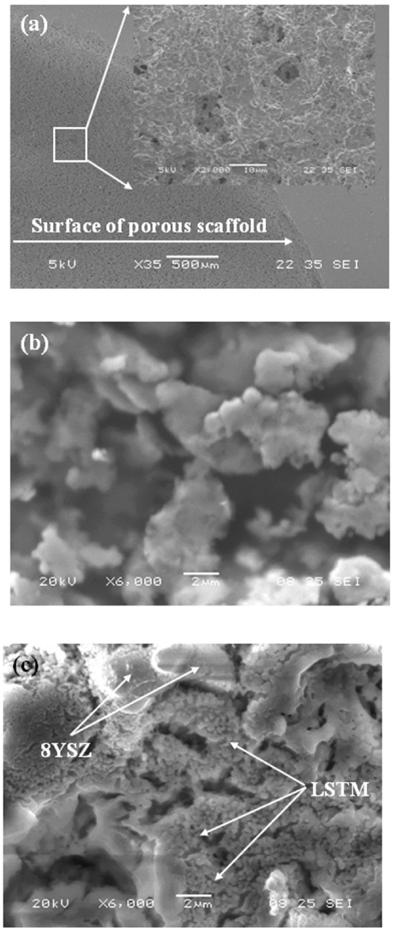

Figure 2. Scanning electron microscopy (SEM) images of LSTM impregnated into a porous 8YSZ scaffold: (a) 8YSZ electrolyte−porous surface of single cell and magnified porous scaffold, (b) surface images of LSTM impregnated at 1200 °C under air, and (c) surface section image of LSTM exposed to humidified H_2 at 800 °C.

for 5 h in air. The bars were then impregnated with LSTM, using the same method as that used for the SOFC anode. The conductivities of the samples were measured using a four-terminal DC arrangement in a custom jig with a Keithley Model 2400 source meter over a temperature range of 50−900 °C at a rate of 5 K min^{-1} in a 5% H_2−Ar or air atmosphere.

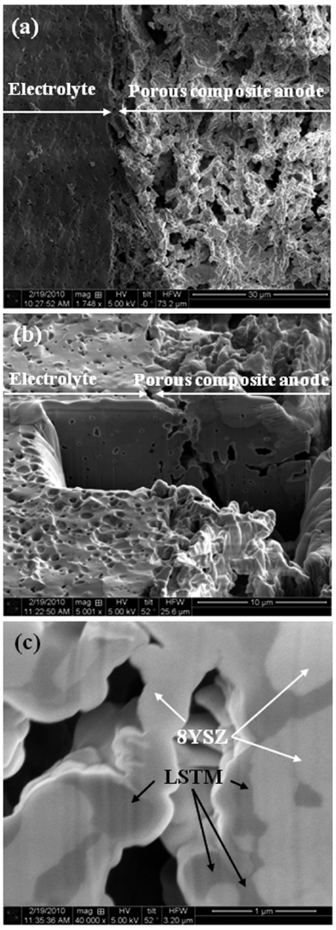

Figure 3. Scanning electron microscopy (SEM) images from the FIB technique: (a) interface image comprised of dense 8YSZ electrolyte (right) and LSTM impregnated into a porous 8YSZ scaffold (left); (b) 3D image of the interface obtained by sectioning with a Ga^+ ion beam; and (c) enlarged image after Ga^+ ion milling.

Voltage, current, and power density properties of the tape-cast SOFC were measured using Solatron Models 1287 and 1255 with a four-lead configuration. H_2 humidified with 3% H_2O was supplied by bubbling through deionized water to the anode side at a flow rate of 30 standard cubic centimeters per minute (30 sccm) for the anode side, and air was fed into the cathode side of SOFC single cell. Silver paste was used for current collection at the cathode and anode surface.

3. RESULTS AND DISCUSSION

To investigate the effect of the calcination temperature on the phase formation of the $La_{0.4}Sr_{0.6}Ti_{0.8}Mn_{0.2}O_{3\pm\delta}$ within the 8YSZ, impregnated samples calcined at a range of temperatures were analyzed by XRD. The resulting XRD patterns are shown in Figure 1. These results show that the single-phase LSTM was determined to form at temperatures of 500 °C and above.[45] The LSTM diffraction peak in the region of $2\theta = 30°-35°$ was much broader for calcining temperatures of <900 °C. This may indicate that the LSTM particles formed at low calcination temperatures are nanoscale or inhomogeneous. At low angles, there are weak peaks of an impurity phase that disappears between 900 °C and 1200 °C. No evidence of phases due to a chemical reaction

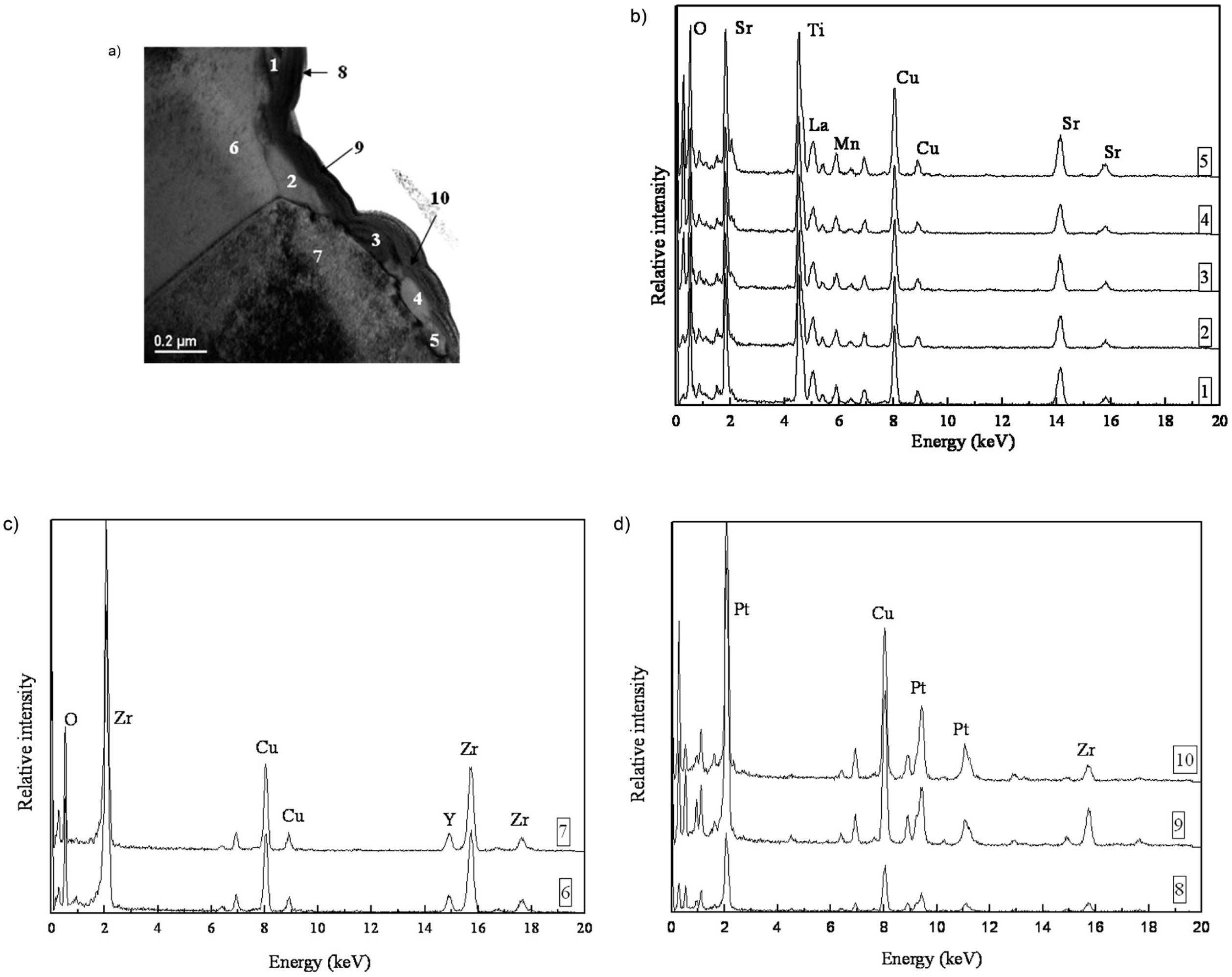

Figure 4. (a) Bright-field TEM image of the LSTM particles on YSZ from an anode exposed to humidified H_2 at 800 °C. The numbers indicate the locations where EDX analysis was performed. These results are shown in panels b, c, and d. Points "1"–"5" correspond to LSTM particles, "6" and "7" denote the 8YSZ substrate, and "8"–"10" originate from a platinum layer.

between 8YSZ and LSTM was found after calcination at 1200 °C for 4 h.

The microstructure of unimpregnated 8YSZ scaffold and LSTM-impregnated 8YSZ in the as-calcined and reduced states are shown in Figure 2. When the porous 8YSZ scaffold in Figure 2a is compared to the impregnated sample in Figure 2b, the presence of the LSTM coating on the YSZ is clearly evident. When the reduced microstructure shown in Figure 2c is compared to the as-calcined structure in Figure 2b, it is clear that major morphological changes have occurred upon reduction. The surface of the LSTM and 8YSZ anode has transformed into a network of very fine particles. These fine LSTM particles are located between and across the surfaces of the 8YSZ scaffold. Similar results can be seen for $La_{0.8}Sr_{0.2}Cr_{0.5}Mn_{0.5}O_3$ (LSCM),[44] where the formation of small particles on the 8YSZ scaffold created a relatively porous structure that should result in an increased triple-phase-boundary (TPB) length for electrochemical reactions in SOFC applications.

To better investigate the interface between the electrolyte and the porous anode, a dual-beam FIB/SEM was used to mill away and image the interface. The FIB image in Figure 3a shows a porous composite anode of the 8YSZ scaffold with impregnated LSTM material on dense 8YSZ electrolyte. A dense structure is shown in the electrolyte, and relatively porous structure is shown at the anode side in Figure 3b. The cross-sectional image is shown as Figure 3c. The LSTM portion appears relatively dark, while the 8YSZ component is lighter in appearance. The identification of these microstructural features was confirmed by TEM. The bright-field TEM image in Figure 4a shows several sites where the composition has been analyzed by EDX. These results are shown in Figures 4b, 4c, and 4d. The small particles numbered "1", "2", "3", "4", and "5" were identified as containing the elements lanthanum, strontium, titanium, and manganese from EDX analysis, which identifies them as LSTM nanoparticles. The larger features, marked "6" and "7" in the figure, are identified as 8YSZ. Thin layers of platinum (marked "8", "9", and "10" in the figure) were observed to cover the former surface of the anode. This is an artifact of the sample preparation and occurs because of the protective platinum layer deposited on the surface of the sample entering the pores of the anode. Copper peaks are present in the EDX spectra, because of the use of a copper support grid.

In addition, the TEM imaging confirms that the particles of LSTM formed upon reduction are ~200 nm in size and are oval in cross section. The large TPB length that should result from the formation of these particles should result in better electrochemical properties under SOFC operation.

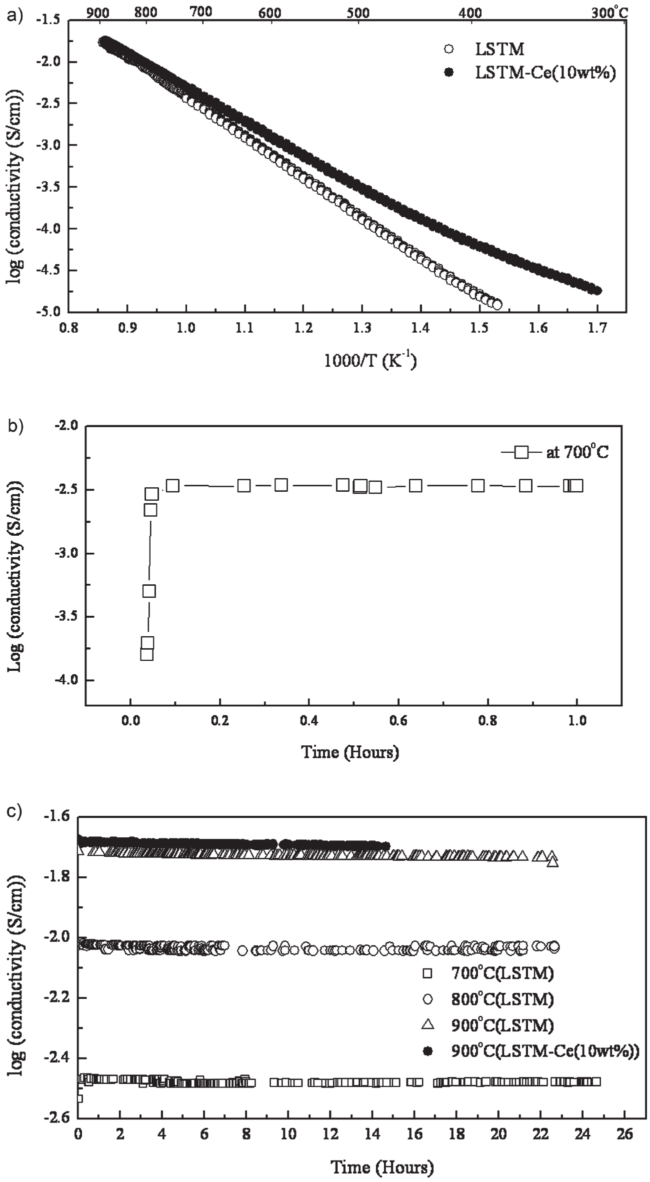

Figure 5. (a) Conductivity of LSTM-8YSZ and LSTM-8YSZ with 10 wt % CeO_2 from room temperature to 900 °C in 5% H_2−Ar ($p_{O_2} = 10^{-19}$ atm). (b) Change in conductivity with time for the in situ reduction of LSTM-8YSZ from an air atmosphere to 5% H_2−Ar at 700 °C. (c) Variation of conductivity with time for LSTM-8YSZ at 700, 800, and 900 °C and LSTM-8YSZ with 10 wt % CeO_2 at 900 °C in 5% H_2−Ar.

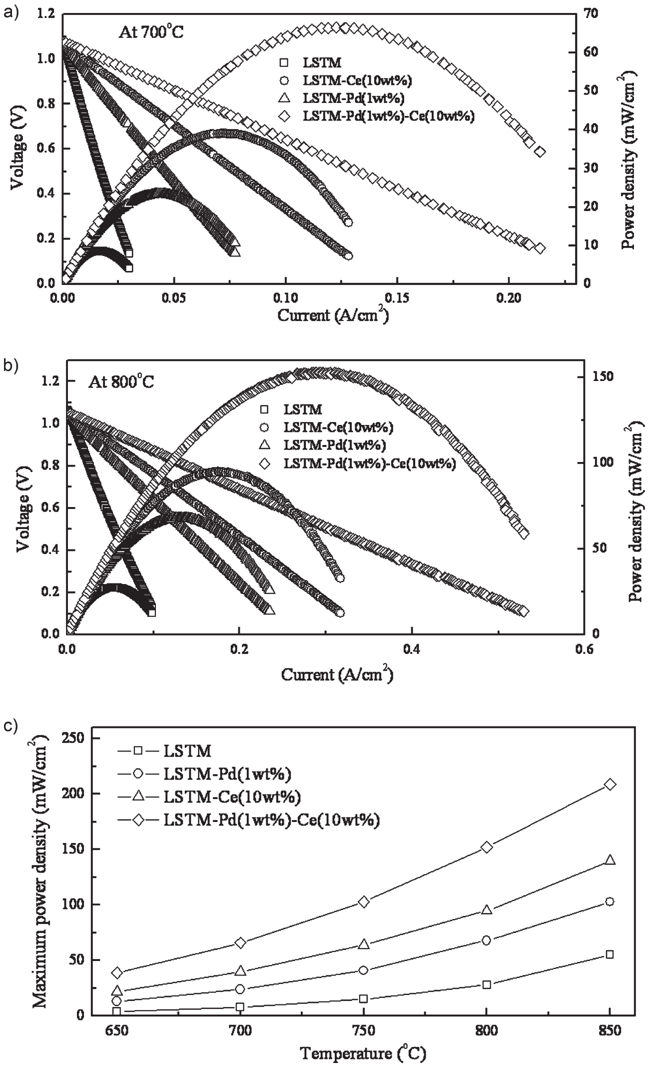

Figure 6. Voltage−current and power density versus current density plots for the cells with each of the four anode compositions at (a) 700 °C and (b) 800 °C. Panel c shows a plot of the maximum power density versus the operating temperature for each of the four anode compositions.

Electrical conductivity measurements were carried out on impregnated LSTM-8YSZ specimens as a function of temperature. The samples analyzed were 8YSZ impregnated with 50 wt % LSTM (LSTM-8YSZ) and 8YSZ impregnated with 50 wt % LSTM plus an additional 10 wt % CeO_2 (LSTM-8YSZ-CeO_2). The electrical conductivity of each sample was measured from room temperature to 900 °C, using the four-probe method, after being pretreated in flowing 5% H_2−Ar at 900 °C (p_{O_2} = 10^{-19} atm). The results of these measurements are shown in Figure 5a. The electrical conductivity of the ceria-containing sample was higher than that of the ceria-free sample across the entire temperature range. Under hydrogen conditions, Ce^{4+} reduces to Ce^{3+} in the oxide, which results in enhanced electronic conductivity.[46,47] The presence of this electrically conducting ceria is thought to lead to an increase in the conductivity, because it increases the connectivity of electrically conducting phases throughout the anode. Upon reduction, Mn and Ti change to lower charge valence states (for example, $Ti^{4+} \rightarrow Ti^{3+}$ and $Mn^{4+} \rightarrow Mn^{3+}$ or Mn^{2+}). The presence of various charge valences (Ti^{4+}/Ti^{3+}, Ce^{4+}/Ce^{3+}, and $Mn^{4+}/Mn^{3+}/Mn^{2+}$) in this oxide system can support a path for better electron transport, as well as provide additional pathways for redox reaction in the LSTM oxide system. Significantly, the presence of the CeO_2 can play a role in making these reactions easier by catalyzing the oxidation process. Figure 5b shows the in situ conductivity results of the reduction of a LSTM-8YSZ sample initially in air at 700 °C. Electrical conductivity increased when hydrogen fuel was supplied to the sample. Significantly, the conductivity increase upon reduction was more rapid than expected, because the large surface area of impregnated materials may improve redox kinetics by facilitating surface exchange. Under hydrogen, there was an increase of two orders of magnitude in the conductivity, compared to that of the oxidized state. Figure 5c shows the long-term conductivity results at 700, 800, and 900 °C under reducing conditions. Conductivity testing of the LSTM-8YSZ scaffold specimen was carried out overnight at a constant temperature with daily increments of 100 °C to investigate the durability of the LSTM anodes. The electrical conductivities of the impregnated LSTM-8YSZ samples at 700, 800, and 900 °C remained constant, indicating good stability. Significantly, the values of 10-wt %-CeO_2-impregnated LSTM-8YSZ sample are also stable over time.

Figure 6 shows voltage, current, and power density properties for four tape-cast SOFC cells fabricated by impregnation of LSTM with CeO_2 and Pd with Ag current collectors. The measurements from these cells at 700 °C are shown in Figure 6a. Their open circuit voltage (OCV) values were ~1.07−1.08 V, which were very close to the theoretical value calculated from the Nernst equation. Such high OCV values indicate that a dense structure is well-formed in the YSZ electrolyte and leakage of the fuel gas is negligible for each sample. As seen in Figure 6a, the power density using a Pd catalyst increased from 10 mW cm^{-2} to 24 mW cm^{-2} at 700 °C. When 10 wt % of CeO_2 was impregnated together with LSTM, the power density was 40 mW cm^{-2}. This is because the added ceria enhanced the conductivity, as well as extended effective active areas. The sample with 10 wt % CeO_2 and 1 wt % Pd with LSTM showed a relatively high power density of 67 mW cm^{-2} at 700 °C. The influence of the catalyst on LSTM at 800 °C in Figure 6b was the same as that at 700 °C. The performance of these cells compare favorably with other similar SOFC with anodes containing strontium-titanate-related phases with and without added ceria catalysts. At 800 °C, the power density of the palladium- and ceria-free single cell was 30 mW cm^{-2}, which exceeds the 20 mW cm^{-2} value reported for $La_{0.3}Sr_{0.7}TiO_3$ (LST)-YSZ/YSZ/$La_{0.8}Sr_{0.2}FeO_3$-YSZ single cell and the 12 mW cm^{-2} value reported for $Sr_{0.88}Y_{0.08}TiO_{3-\delta}$ (YST)/YSZ/LSM.[25,48] The power density of 10 wt % CeO_2 with LSTM cell was 100 mW cm^{-2} at 800 °C, which is again higher than the 63 mW cm^{-2} value reported when 10 wt % CeO_2 is added to the YST/YSZ/LSM cell.[25]

The power density, with respect to the temperature, for the four SOFC systems studied is shown in Figure 6c. In all four SOFC systems studied, there is an increase in the maximum power with increasing temperature. The addition of palladium or ceria catalysts improves performance across the entire temperature range studied. The cell containing 10 wt % CeO_2 outperforms the cell containing 1 wt % Pd; however, the combination of both catalysts provides the highest power density. The highest power density achieved in this study were for the cell containing 10 wt % CeO_2 and 1 wt % Pd, with 150 mW cm^{-2} at 800 °C and 210 mW cm^{-2} at 850 °C. These high powder densities are achieved because palladium and ceria are two of the most active materials for effective catalysis of the different processes in fuel oxidation.

4. CONCLUSIONS

It was possible to fabricate composite anodes of 8YSZ and LSTM by impregnating a porous scaffold of 8YSZ with an aqueous solution. The impregnated LSTM was synthesized at temperatures over 700 °C and did not react with 8YSZ at 1200 °C. The impregnated LSTM formed a continuous layer on the porous 8YSZ surface under oxidizing conditions; however, when reduced, the LSTM layer transformed to an interconnected network of nanoscale fine particles. The electrical conductivities of LSTM-8YSZ and LSTM-8YSZ-CeO_2 were stable at 700, 800, and 900 °C. Tape-cast SOFCs with impregnated LSTM exhibited excellent performance when CeO_2 and Pd were used as catalysts.

AUTHOR INFORMATION

Corresponding Author

*Tel.: +44-1334-463817. Fax: +44-1334-463808. E-mail: jtsi@st-andrews.ac.uk.

ACKNOWLEDGMENT

The authors are grateful for the support given by the Research Councils United Kingdom (RCUK) Energy program. In addition, we thank the Engineering and Physical Sciences Research Council (EPSRC) of the United Kingdom for Senior Fellowship and U.S. Office of Naval Research for project support.

REFERENCES

(1) Steele, B. C. H. *Nature* **1999**, *400*, 619.
(2) Singhal, S. C. *Solid State Ionics* **2000**, *135*, 305.
(3) Juhl, M.; Primdahl, S.; Manon, C.; Mogensen, M. *J. Power Sources* **1996**, *61*, 173.
(4) Murry, E. P.; Barnett, S. A. *Solid State Ionics* **2001**, *143*, 265.
(5) Takeda, Y.; Kanno, R.; Noda, M.; Tomida, Y.; Yamamoto, O. *J. Electrochem. Soc.* **1987**, *134*, 2656.
(6) Jiang, S. P.; Chan, S. H. *Mater. Sci. Technol.* **2004**, *20* (9), 1109.
(7) Kim, J.-W.; Virkar, A. V.; Mehta, K.; Fung, K.-Z.; Singhal, S. C. *J. Electrochem. Soc.* **1999**, *146* (1), 69.
(8) Trembly, J. P.; Marquez, A. I.; Ohrn, T. R.; Bayless, D. J. *J. Power Sources* **2006**, *158*, 263.
(9) Matsuzaki, Y.; Yasuda, I. *Solid State Ionics* **2000**, *132*, 261.
(10) Zha, S. W.; Cheng, Z.; Liu, M. L. *J. Electrochem. Soc.* **2007**, *154*, B201.
(11) Sarantaridis, D.; Atkinson, A. *Fuel Cells* **2007**, *7*, 246.
(12) Atkinson, A.; Barnett, S.; Gorte, R. J.; Irvine, J. T. S.; McEvoy, A. J.; Mogensen, M.; Singhal, S. C.; Vohs, J. *Nature Mat.* **2004**, *3*, 17.
(13) Horita, T.; Yamaji, K.; Kato, T.; Kishimoto, H.; Xiong, Y.; Sakai, N.; Brito, M. E.; Yokokawa, H. *J. Power Sources* **2005**, *145*, 133.
(14) Horita, T.; Yamaji, K.; Kato, T.; Sakai, N.; Yokokawa, H. *Solid State Ionics* **2004**, *172*, 93.
(15) Horita, T.; Yamaji, K.; Kato, T.; Sakai, N.; Yokokawa, H. *J. Power Sources* **2004**, *131*, 299.
(16) Sasaki, K.; Watanabe, K.; Shiosaki, K.; Susuku, K.; Teraoka, Y. *J. Electroceram.* **2004**, *13*, 669.
(17) Ringuedè, A.; Labrincha, J. A.; Frade, J. R. *Solid State Ionics* **2001**, *141−142*, 549.
(18) Vernoux, P.; Guillodo, M.; Fouletier, J.; Hammou, A. *Solid State Ionics* **2000**, *135*, 425.
(19) Gorte, R. J.; Kim, H.; Vohs, J. M. *J. Power Sources* **2002**, *106*, 10.
(20) Lu, C.; Worrell, W. L.; Wang, C.; Park, S.; Kim, H.; Vohs, J. M.; Gorte, R. J. *Solid State Ionics* **2002**, *152−153*, 393.
(21) Lu, C.; An, S.; Worrell, W. L.; Vohs, J. M.; Gorte, R. J. *Solid State Ionics* **2004**, *175*, 47.
(22) An, S.; Lu, C.; Worrell, W. L.; Gorte, R. J.; Vohs, J. M. *Solid State Ionics* **2004**, *175*, 135.
(23) Costa-Nunes, O.; Gorte, R. J.; Vohs, J. M. *J. Power Sources* **2005**, *141*, 241.
(24) Gross, M. D.; Vohs, J. M.; Gorte, R. J. *Electrochim. Acta* **2007**, *52*, 1951.
(25) He, H.; Huang, Y.; Vohs, J. M.; Gorte, R. J. *Solid State Ionics* **2004**, *175*, 171.
(26) Jiang, S. P.; Chen, X. J.; Chan, S. H.; Kwok, J. T.; Khor, K. A. *Solid State Ionics* **2006**, *177*, 149.

(27) Zhu, W. Z.; Deevi, S. C. *Mater. Sci. Eng. A* **2003**, *362*, 228.

(28) Zhan, Z.; Barnett, S. A. *Solid State Ionics* **2005**, *176*, 871.

(29) Takeguchi, T.; Kani, Y.; Yano, T.; Kikuchi, R.; Eguchi, K.; Tsujimoto, K.; Uchida, Y.; Ueno, A.; Omoshiki, K.; Aizawa, M. *J. Power Sources* **2002**, *112*, 588.

(30) Yoon, S. P.; Han, J.; Nam, S. W.; Lim, T.-H.; Hong, S.-A. *J. Power Sources* **2004**, *136*, 30.

(31) McIntosh, S.; Vohs, J. M.; Gorte, R. J. *Electrochim. Acta* **2002**, *47*, 3815.

(32) Lü, Z.; Pei, L.; He, T.-M.; Huang, X.-Q.; Liu, Z.-G.; Ji, Y.; Zhao, X.-H.; Su, W.-H. *J. Alloys Compd.* **2002**, *334*, 299.

(33) Takeguchi, T.; Kikuchi, R.; Yano, T.; Eguchi, K.; Murata, K. *Catal. Today* **2003**, *84*, 217.

(34) Kishimoto, H.; Yamaji, K.; Horita, T.; Xiong, Y.; Sakai, N.; Brito, M. E.; Yokokawa, H. *J. Power Sources* **2007**, *172*, 67.

(35) Jung, S.; Gross, M. D.; Gorte, R. J.; Vohs, J. M. *J. Electrochem. Soc.* **2006**, *153*, A1539.

(36) Sfeir, J. *J. Power Sources* **2003**, *118*, 276.

(37) Aguilar, L.; Zha, S.; Cheng, Z.; Winnick, J.; Liu, M. *J. Power Sources* **2004**, *135*, 17.

(38) Perry Merray, E.; Tsai, T.; Barnett, S. A. *Nature* **1999**, *400*, 649.

(39) Yaremchenko, A. A.; Valente, A. A.; Kharton, V. V.; Bashmakov, I. A.; Rocha, J.; Marques, F. M. B. *Catal. Commun.* **2003**, *4*, 477.

(40) Modafferi, V.; Panzera, G.; Baglio, V.; Frusteri, F.; Antonucci, P. L. *Appl. Catal., A* **2008**, *334*, 1.

(41) Kim, H.; Lu, C.; Worrell, W. L.; Vohs, J. M.; Gorte, R. J. *J. Electrochem. Soc.* **2002**, *149* (3), A247.

(42) Kim, G.; Corr, C.; Irvine, J. T. S.; Vohs, J. M.; Gorte, R. J. *Electrochem. Solid-State Lett.* **2008**, *11*, B16.

(43) Corre, G.; Kim, G.; Cassidy, M.; Vohs, J. M.; Gorte, R. J.; Irvine, J. T. S. *Chem. Mater.* **2009**, *21*, 1077.

(44) Kim, G.; Lee, S.; Shin, J. Y.; Irvine, J. T. S.; Vohs, J. M.; Gorte, R. J. *Electrochem. Solid-State Lett.* **2009**, *12*, B48.

(45) Fu, Q. X.; Tietz, F.; Stover, D. *J. Electrochem. Soc.* **2006**, *153*, D74.

(46) Inaba, H.; Tagawa, H. *Solid State Ionics* **2000**, *83*, 1.

(47) Balducci, G.; Islam, M. S.; Kašpar, J.; Fornasiero, P.; Graziani, M. *Chem. Mater.* **2003**, *15*, 3781.

(48) Lee, S.; Kim, G.; Vohs, J. M.; Gorte, R. J. *J. Electrochem. Soc.* **2008**, *155*, B1179.